



UNIVERSITY OF LEEDS

This is a repository copy of *Self-Nano-Structuring in SrTiO₃: A Novel Strategy for Enhancement of Thermoelectric Response in Oxides*.

White Rose Research Online URL for this paper:
<http://eprints.whiterose.ac.uk/150585/>

Version: Accepted Version

Article:

Azough, F, Gholinia, A, Alvarez-Ruiz, DT et al. (5 more authors) (2019)
Self-Nano-Structuring in SrTiO₃: A Novel Strategy for Enhancement of Thermoelectric Response in Oxides. ACS Applied Materials & Interfaces, 11 (36). pp. 32833-32843. ISSN 1944-8244

<https://doi.org/10.1021/acsami.9b06483>

(c) 2019, American Chemical Society. This is an author produced version of a paper published in ACS Applied Materials & Interfaces. Uploaded in accordance with the publisher's self-archiving policy.

Reuse

Items deposited in White Rose Research Online are protected by copyright, with all rights reserved unless indicated otherwise. They may be downloaded and/or printed for private study, or other acts as permitted by national copyright laws. The publisher or other rights holders may allow further reproduction and re-use of the full text version. This is indicated by the licence information on the White Rose Research Online record for the item.

Takedown

If you consider content in White Rose Research Online to be in breach of UK law, please notify us by emailing eprints@whiterose.ac.uk including the URL of the record and the reason for the withdrawal request.



eprints@whiterose.ac.uk
<https://eprints.whiterose.ac.uk/>

Self-Nano-Structuring in SrTiO₃: A Novel Strategy for Enhancement of Thermoelectric Response in Oxides

Feridoon Azough¹, Ali Gholinia¹, Diana T. Alvarez -Ruiz¹, Ercin Duran¹
Demie M. Kepaptsoglou^{2,3}, Alexander S. Eggeman¹, Quentin M. Ramasse^{2,4}
and Robert Freer^{1,*}

¹School of Materials, University of Manchester, Manchester, M13 9PL, U.K.

²SuperSTEM Laboratory, STFC Daresbury Campus, Daresbury WA4 4AD, U.K.

³Jeol Nanocentre and Department of Physics, University of York, Heslington, York
YO10 5DD, U.K.

⁴School of Chemical and Process Engineering and School of Physics, University of Leeds,
Leeds LS2 9JT, U.K.

[*Robert.Freer@manchester.ac.uk](mailto:Robert.Freer@manchester.ac.uk)

Abstract:

Nano-structuring is recognised as an efficient route for enhancing thermoelectric response. Here we report a new synthesis strategy for nanostructuring oxide ceramics and demonstrate its effectiveness on an important n-type thermoelectric SrTiO₃. Ceramics of Sr_{0.9}La_{0.1}TiO₃ with additions of B₂O₃ were synthesized by the mixed oxide route. Samples were sintered in air followed by annealing in a reducing atmosphere. Crystallographic data from X-ray and electron diffraction showed $Pm\bar{3}m$ cubic symmetry for all the samples. High resolution transmission electron microscopy (HRTEM) showed the formation of a core-shell type structure within the grains for the annealed ceramics. The cores contain nanosize features comprising pairs of nano-size voids and particles; the feature sizes depend on annealing time. Atomic-resolution, high-angle annular-dark-field imaging and electron energy loss spectroscopy in the scanning transmission electron microscopy (STEM-HAADF-EELS) showed the particles to be rich in Ti and the areas around the voids to contain high concentrations of Ti³⁺. Additionally, dislocations were observed, with significantly higher densities in the shell areas. The observed dislocations are combined (100) and (110) edge dislocations. The major impact of the core-shell type microstructures, with nano-size inclusions, is the reduction of the thermal conductivity. Sr_{0.9}La_{0.1}TiO₃ ceramics containing grain boundary shells of size $\approx 1 \mu\text{m}$ and inclusions in the core of 60 to 80 nm exhibit a peak power factor of 1600 $\mu\text{W}/\text{m}\cdot\text{K}^2$ at 540 K; at 1000 K they exhibit a low thermal conductivity (2.75 W/m.K) and a power factor of 1050 $\mu\text{W}/\text{m}\cdot\text{K}^2$ leading to a high of ZT of 0.39 ± 0.03 . This is the highest ZT reported so far for Sr_{0.9}La_{0.1}TiO₃ based-compositions. This nanostructuring strategy should be readily applicable to other functional oxides.

Keywords: Nanostructuring, Thermal conductivity, Strontium Titanate, Oxide thermoelectric, Perovskite, Aberration Corrected Microscopy, 3D Electron Diffraction

Introduction:

The considerable amounts of heat wasted every day in industrial, commercial and domestic environments provide important opportunities for thermoelectric generators to convert some of this heat into usable electric power¹⁻³. Thermoelectric generators make use of materials whose thermoelectric performance is characterized by the dimensionless figure of merit, $ZT = (S^2\sigma T/k)$, where S is the Seebeck coefficient, σ the electrical conductivity and k the

thermal conductivity. Over the last two decades, improvements of the ZT value have been achieved in traditional thermoelectric materials and to some extent in newly developed oxide thermoelectrics by micro- and nano-structuring of the materials^{1,4-7} Part of the driving force for nanostructuring has been the need to decouple the closely related material properties S , σ and k and thereby increase the thermoelectric figure of merit, ZT beyond that in normal bulk materials⁸⁻¹².

For many nanostructured bulk materials, the enhancement in the value of ZT can be attributed to a significant reduction in the lattice thermal conductivity as a result of changes in structure and local chemistry, which give rise to a high density of phonon-scattering interfaces¹³. However, the introduction of such interfaces can be counterproductive, as it will generally result in a significant reduction of the electrical conductivity². An alternative approach for the reduction of thermal conductivity is by the fabrication of nanocomposite structures, for instance by compaction of the main material with nanosize inclusions, or by in-situ nano-inclusion formation by means of precipitation¹⁴⁻¹⁶. Here, the main role of nano-inclusions is to generate additional phonon scattering centres without severely reducing the bulk electrical conductivity. The size, shape and volume fraction of the nanoparticles have a significant influence on the scattering efficiency,¹⁷. However, it is reported that inclusions could increase electrical conductivity while reducing thermal conductivity¹⁸. The general approach for nanostructuring thermoelectrics involves the introduction of nanosized features such as voids, particles with round or faceted morphology, atomic scale platelets dispersed within the grains or the grain boundaries of the bulk material to reduce thermal conductivity. In traditional thermoelectrics, significant ZT improvements have been achieved in many systems; in half-Heusler alloys by adding nano-ZrO₂¹⁹, in Bi₂Te₃ by adding nano-SiC particles²⁰, and in Yb_{0.2}Co₄Sb_{12+y} by dispersing in situ partially oxidized Yb₂O₃ nanoparticles²¹ It is also has been reported that more significant enhancements can be achieved by embedding metal or conductive nanoparticles into the matrix: examples include lead and antimony in PbTe²² antimony in Yb_yCo₄Sb₁₂²³.

Metal oxides have great potential as thermoelectric materials for high temperature applications, with SrTiO₃ being considered one of the most promising n-type oxides^{2,24}. It crystallizes in a simple cubic Pm $\bar{3}$ m perovskite structure, has a high S value of 600 μ V/K and is normally utilised as an insulator. However, by doping the Sr sites with lanthanides or the Ti sites with Nb, it becomes an n-type semiconductor^{25,26}. The thermoelectric power factor,

$S^2\sigma$, of La-doped single-crystal strontium titanate is comparable with that of traditional thermoelectric materials such as Bi_2Te_3 ,². Despite these excellent electronic transport properties, the lattice thermal conductivity of SrTiO_3 is comparatively high, limiting its usability for practical applications. Various strategies have been employed to reduce the thermal conductivity of SrTiO_3 ceramics including controlling the grain size^{27,28}, introducing nano-size inclusions by SPS,²⁹ introducing conductive metallic particles within the matrix³⁰, co-doping of A-site with Lanthanides³¹, creation of A-site vacancies³² and nano-scale modulation doping³³. The thermoelectric properties of A-site doped SrTiO_3 with 10 mole% lanthanides ($\text{Sr}_{0.9}\text{Ln}_{0.1}\text{TiO}_3$ = La, Nd, Y and Pr) look very promising and have been extensively studied^{25,34–36}. However, these compositions require high sintering temperatures above 1600°C to achieve high sample densities, which could limit scalability as industrially-viable thermoelectrics. For some years B_2O_3 has been used to lower the sintering temperature of a variety of electroceramics³⁷. Additionally, it has been shown that B-doping of SrTiO_3 simultaneously increases the Seebeck coefficient and the electrical conductivity³⁸.

Here, we present a novel strategy for self-nanostructuring in oxide ceramics and demonstrate its effectiveness for optimising the transport properties of strontium titanate based thermoelectrics. Through the use of different sintering atmospheres, a distinct core-shell grain microstructure is achieved. In turn, the core of the formed grains is itself nano-structured, comprising a matrix surrounding uniformly distributed pairs of nano-size precipitates and voids. Atomic level imaging and chemical characterization, using scanning transmission electron microscopy (STEM), high-angle annular dark field (HAADF), and electron energy loss spectroscopy (EELS) has been employed to investigate the microstructural changes that occur in $\text{Sr}_{0.9}\text{Ln}_{0.1}\text{TiO}_3$ upon annealing in a reducing atmosphere, with a particular focus on the formation of these core-shell type structures containing pairs of voids and inclusions and how they affect the thermoelectric response of the material. This approach to controlling the nanostructure of thermoelectrics could find much wider applicability in the routes to synthesise future target materials and achieving higher performance.

Experimental:

Ceramics of $\text{Sr}_{0.9}\text{La}_{0.1}\text{TiO}_3$ were produced by the standard mixed oxide route. All powders were of 99.9% purity and obtained from Sigma Aldrich. The La_2O_3 was first dried at 1173 K

for 6 h prior to mixing with TiO_2 and SrCO_3 in the required ratios. The powders were wet mixed in a vibratory mill for 24 h with yttrium oxide stabilized zirconia balls and propan-2-ol. After drying, the powders were calcined for 8 h at 1473 K in air atmosphere. B_2O_3 (0.6 wt %) was added to the calcined powders and the mixtures were re-milled (under the conditions described above), and dried before pressing uniaxially in a 20 mm die at 50 MPa. The pellets were sintered at 1723 K for 4 h in air and then cooled at 633 K. Subsequently, the sintered samples were annealed under a reducing atmosphere (Ar 5% - H_2) at 1623 K for periods of 12 h to 48 h. After determining the densities by the Archimedes method, the samples were cut and their microstructures, crystal structures and thermoelectric responses evaluated.

X-ray diffraction (XRD) was performed with a Philips X'Pert Pro diffractometer with 0.005° step size (20 s per step) between 5° and 100° . Rietveld analysis of the data was undertaken using TOPAS 4.2 software (Bruker AXS, Karlsruhe, Germany)³⁹. The microstructures of the samples were analyzed using a Philips XL30 and a TESCAN field emission gun (FEG)-SEM, both equipped with an energy-dispersive X-ray detector. Samples for transmission electron microscopy (TEM) and STEM observation were prepared by both standard crushing and ion beam-thinning techniques. whereby sintered disks were crushed to a powder using an agate mortar and pestle. Grains of individual powders were dispersed in chloroform, dropped onto a copper grid covered with a holey carbon film, and then dried. Structures were initially investigated using selected area electron diffraction (SAED) and HRTEM techniques using a FEI FEGTEM (Tecnai G2, Hillsboro, OR) operating at 300 kV. Subsequently, atomic level resolution level structural characterization was carried out using an aberration-corrected Nion microscope (UltraSTEM100; Nion Company, Kirkland, WA), located at the Daresbury SuperSTEM Laboratory in the United Kingdom. Electron diffraction tomography was performed using the same microscope and settings as above. Diffraction patterns were recorded at consecutive tilt steps from -70° to $+70^\circ$ at 2° increments. The reciprocal lattice reconstructions were performed using the PETS diffraction tomography platform⁴⁰.

The Seebeck coefficient, S , and electrical conductivity, σ , were measured simultaneously at temperatures up to 1000 K, in a helium atmosphere, using a ULVAC ZEM 3. Thermal conductivity was obtained from measurements of the density, the thermal diffusivity (custom-built apparatus in an argon atmosphere), and heat capacity (Netzsch STA 449 C); the latter two measurements were carried out in an Ar atmosphere.

Results and Discussion:

Structural Bulk Properties.

Sintering of lanthanide substituted strontium titanate with excess lanthanides, i.e. $\text{Sr}_{0.9}\text{Ln}_{0.1}\text{TiO}_3$ (Ln = La, Nd and Pr), in air atmosphere requires high temperatures of 1900 K and above²⁵. However, high density ($\geq 95\%$ theoretical) crack-free samples of $\text{Sr}_{0.9}\text{Ln}_{0.1}\text{TiO}_3$ (hereafter denoted L10) were produced by sintering at the much lower temperature of 1723 K with the aid of 0.6 wt% additions of B_2O_3 . The air sintered L10 samples were light grey in color; after subsequent annealing under reducing conditions the samples were black in colour with marginally lower density, but generally 95% theoretical and above. The change in colour from grey to black reflects the increasing content of Ti^{+3} ^{31,41} as a result of sintering under reducing conditions.

Phase Analysis

X-ray Diffraction

XRD spectra of L10 samples sintered in air and then annealed at 1350°C for different times are shown in Figure 1a. For convenience, these samples will be referred to as 0h, 12h, 24h, 32h and 48h, respectively, where 0h represents air-sintered samples and the numbers (12 to 48) represent the annealing time in hours. Topas refinement of all XRD spectra confirmed the cubic, $\text{Pm}\bar{3}\text{m}$ space group for all samples. With increasing the annealing time under Ar-5\%H_2 atmosphere, the XRD diffraction peaks move to lower diffraction angles, reflecting a small overall increase in the lattice parameter of the cubic phase, as shown in Figure 1b. The larger lattice parameter can be explained by the formation of Ti^{3+} to compensate for excess electrons from oxygen vacancies created during annealing under reducing conditions^{31,36}; Ti^{3+} ions have a larger atomic radius (0.81 Å) than Ti^{4+} ions (0.74 Å) in the TiO_6 octahedra⁴². These changes in lattice parameter due to reduction are consistent with previous investigations of perovskite materials sintered in different environments⁴³. All the XRD spectra showed three minor extra diffraction peaks at 2 theta of 28.9, 31.5 and 35.5. These peaks can be indexed as the $\text{Sr}_3\text{Ti}_2\text{O}_7$ Ruddlesden Popper phase⁴⁴ which is present here as a minority secondary phase. It is believed that Boron dissolves in $\text{Sr}_{0.9}\text{La}_{0.1}\text{TiO}_3$ in the final stage of the liquid phase sintering⁴⁵ causing the solubility limit to be exceeded and thereby forming the $\text{Sr}_3\text{Ti}_2\text{O}_7$ Ruddlesden Popper secondary phase⁴⁶.

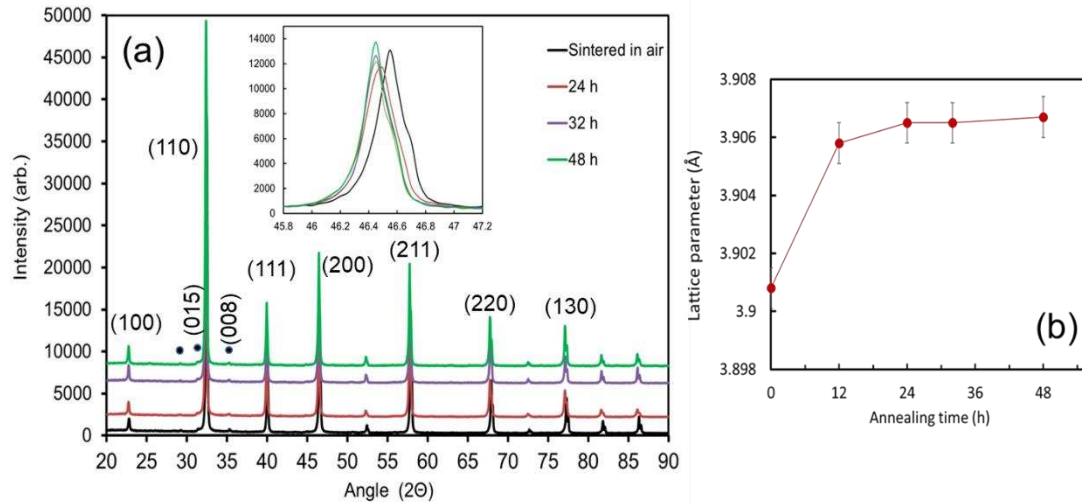


Figure 1. (a) XRD spectra for L10 samples sintered in air and annealed in Ar - 5% H_2 atmosphere for different times; black, red, purple and green spectra correspond to air-sintered, and annealed under reducing conditions for 24h,32h and 48 h, respectively. The inset shows the (200) peak shift as a function of annealing time. (b) Refined lattice parameters of the samples after annealing.

Microstructure evaluation

Scanning Electron Microscopy

To evaluate the sample microstructures after sintering and annealing SEM characterization was initially performed. Figure 2a presents the microstructure of the air sintered samples; it exhibits regular polygonal-shaped grains with average size $\sim 7 \pm 0.2 \mu\text{m}$. No sub-grain features were observed in the microstructures of the air sintered samples or the samples annealed for 12 h under a reducing atmosphere; the microstructures of both types of samples, in terms of grain size and shape, were very similar (as an example Figure S-1 in Supporting Information shows the microstructure of a sample annealed for 12 h). However, a major change in the microstructure was observed after annealing samples for 24 h or longer under reducing atmosphere: a core-shell type composite microstructure developed within the grains (Figure 2b). The grain shell appears as a bright band along the grain boundaries, while the grain core shows darker contrast compared to that of the shell. The thickness of the shell was uniform, being typically $1.0 \mu\text{m}$ and $1.6 \mu\text{m}$ for the samples annealed for 24 and 32 hours respectively. On further increasing the annealing time to 48 hours, the core-shell microstructure was still present, but the thickness of the shell was less uniform (Figure 2c). In order to explore the chemistry of the composite microstructure, SEM-EDS measurements

were performed (examples given in Supporting Information, Figure S-2 and S-3) and reveal that despite the different core and shell morphologies, the average composition is uniform throughout the newly formed microstructures.

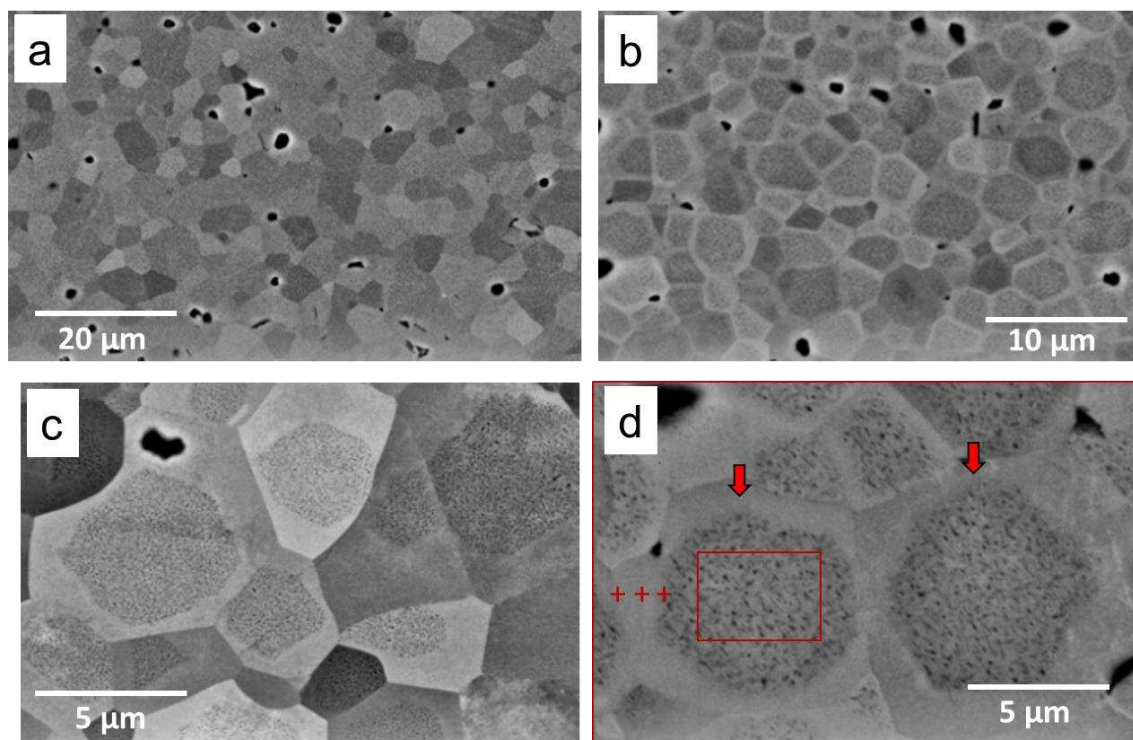


Figure 2. Back scattered electron (BSE) SEM images for L10 samples: (a) sintered in air, (b) sintered in air then annealed in Ar - 5% H_2 for 24 h, (c) SEM image for the sample sintered in air then annealed in Ar - 5% H_2 for 48h, (d) high magnification SEM image of sample annealed for 24 h, the red arrows in the figure highlight the shell areas; crosses and the red box indicate EDS analysis regions – see Supporting Information.

Higher magnification SEM images (acquired at a magnification of 100kx) revealed extra details of the nano size features in the core regions (Figure 3); these were predominantly: (i) elongated, rod-shaped features, having darker contrast at one end, and (ii) dark or bright round dots (Figure 3). The elongated features of varying size, with maximum length of about 200 nm for samples annealed for 48 h, appear to be randomly distributed in the matrix of the core. A number of the rod-shaped features are aligned along the main in-plane crystallographic directions of the matrix, suggesting that the ‘round dots’ could be rod-shaped features aligned vertically along the viewing direction. However, pairs of round dark and bright features with no specific orientation relationship with respect to each other can also be seen, such as those highlighted in Figure 3 inside dashed circles. The length of the rod-shaped features vary in size for each annealing time. The maximum size of rod-shaped features estimated from the BSE-SEM images is 80 nm, 160 nm and 220 nm for annealing times of 24

h, 32 h, and 48 h respectively. The detailed microstructural characteristics of the nano size features, and the orientation relationships between the nano size features and the matrix of the grains, will be discussed in the STEM-EELS section. It should be noted that the minor secondary phase observed in the X-ray diffraction spectra (Figure 1a) appears as needle-shaped features at grain boundaries of the main phase (Figure S-4 of the Supporting Information provided).

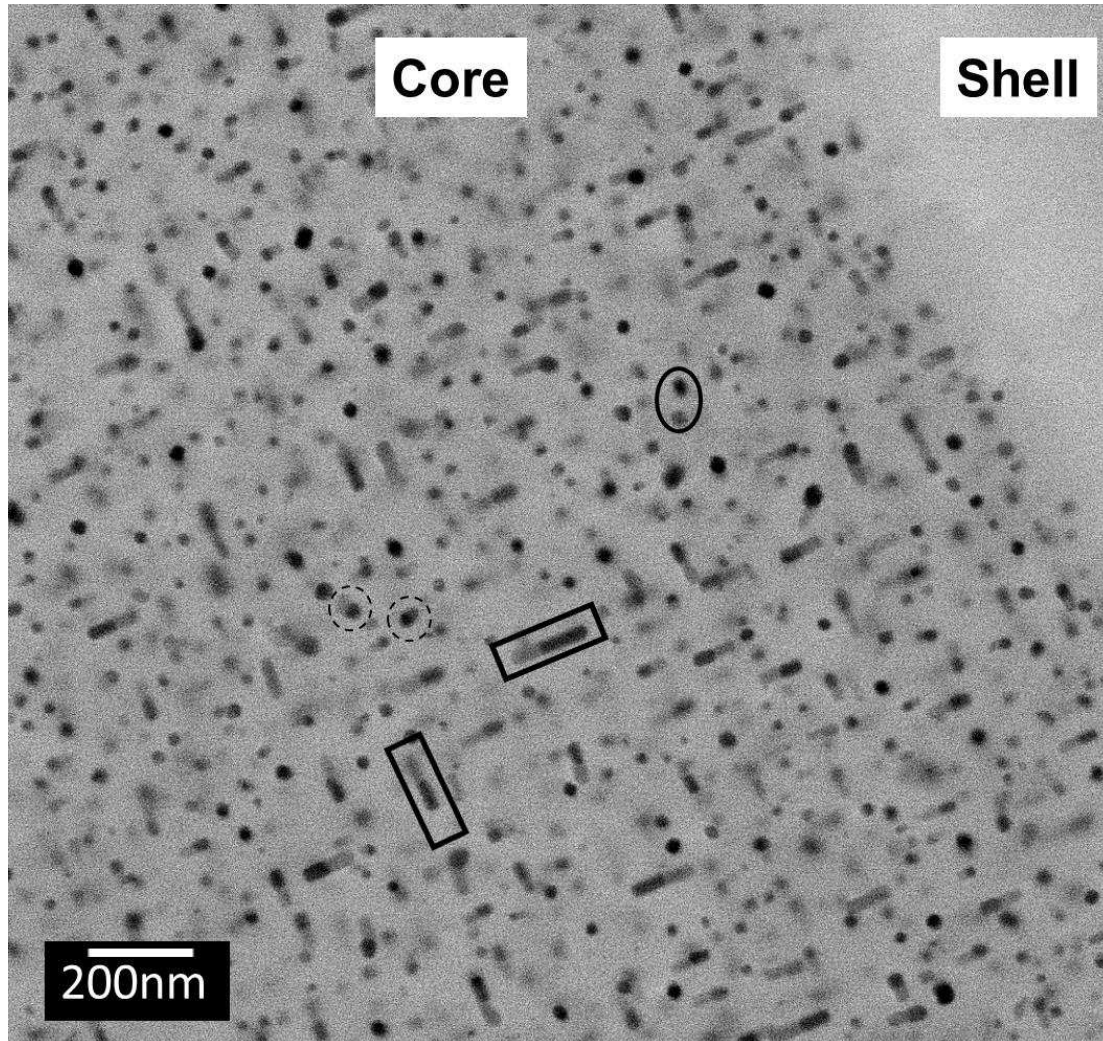


Figure 3. High magnification (100 kx) BSE – SEM image showing the distribution of the nano sized features in the core area of a sample annealed under reducing conditions for 48 h.

Transmission Electron Microscopy.

To provide further insight into the details and nature of the core-shell type structure, conventional TEM and advanced electron microscopy using atomically resolved STEM and EELS was performed. TEM data for the shell and core areas of a L10 sample annealed for 24

h in Ar - 5% H_2 are presented in Figure 4. The presence of a high density of dislocations in the shell area is the main feature of the microstructure in Figure 4a. Some dislocations are also visible in the core area of the sample. Dislocations are common lattice imperfections in un-doped single crystal and polycrystalline $SrTiO_3$ prepared in air⁴⁷⁻⁴⁹. Some of the nano-sized inclusions observed in the SEM microstructure analysis can also be seen in the core area in this micrograph (arrowed, blue in colour). Higher magnification TEM images of the core area for the sample, Figure 4(b, c), show a uniform distribution of inclusions, with sizes ranging from 20 nm to 80 nm. The macroscopic morphology of these inclusions can be broadly described as a 'peanut' or 'dumbbell' shape: closer inspection shows that the inclusions actually comprise two 'sub-structures' (see inset Figure 4b). Commonly, Moire fringes exist in HRTEM images of one of the components as shown in the top left inset of the Figure 4b. Observation of these inclusions in the thinner areas of the TEM sample shows that one part of the inclusions is in fact a nano sized void and the second component is a solid particle precipitate (Figure 4c). Comparison of the Fourier transform (FFT) of the HRTEM images acquired from such particles and the surrounding matrix, shows that the particles and the matrix of the core may differ in structure (Figure 4c). Furthermore, as noted above, much lower densities of dislocations were observed within the cores, but when present, the dislocations were frequently observed to be connecting sets of particle-void pairs.

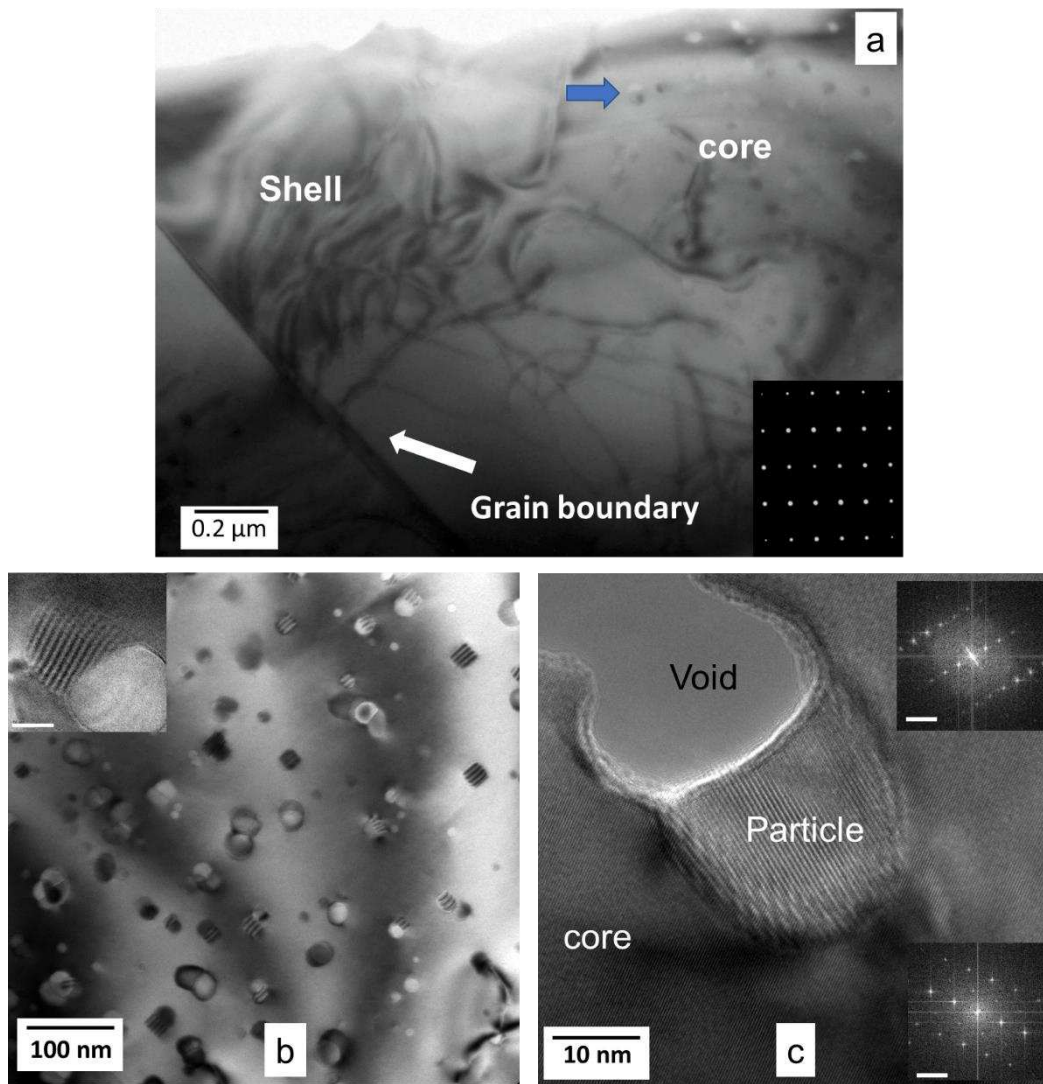


Figure 4. TEM data for a L10 sample sintered in air and then annealed in Ar - 5%H₂ for 24 h (a), [110] zone axis TEM image showing a high density of dislocations in the shell area. (b) Low magnification TEM image of sample. The scale bar in the top left inset represents 20 nm, (c) High magnification TEM of the same sample, the top right and bottom right insets represent FFTs of the particle and the core respectively. The scale bars in the FFTs represent 4 Å in real space.

More detailed analysis of the secondary phase was performed using precession electron diffraction tomography, allowing the complete reciprocal lattice of the crystal structure to be determined. The reciprocal lattice projections were found to be a superstructure of the parent perovskite structure of SrTiO₃ and projections of the crystal structure along one of the perovskite <100> directions and along one of the cubic <110> directions are shown in Figure 5a and 5b respectively. The superlattice reflections between the parent perovskite reflections indicate a much larger unit cell with a volume potentially as large as 1800 Å³ rather than the perovskite cell volume of 64 Å³. The precise atomic arrangement that gives rise to the

structure is still under investigation but the high degree of coherency between this phase and the parent perovskite structure is clear from the reciprocal lattice reconstructions, hence the strong directionality of the nanosized features in Figure 3. The small size of these phases, the relatively weak superstructure reflection intensity and the high degree of coherency suggest that this phase would not be easily identified in the conventional XRD analysis.

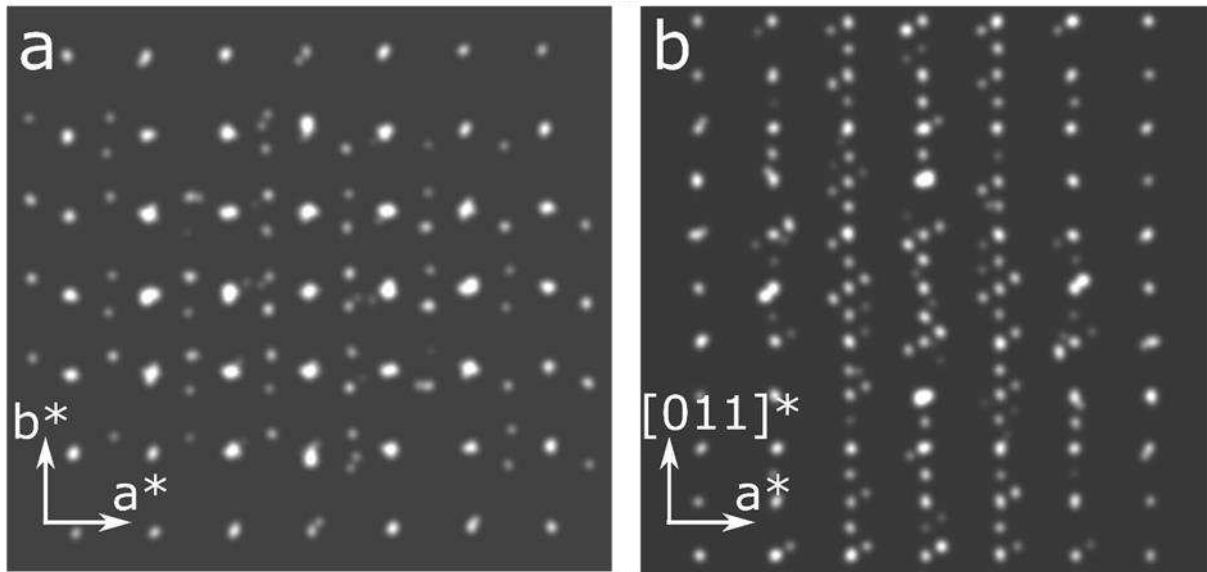


Figure 5. Reciprocal lattice projections of the nanosize precipitate particles viewed along a) the perovskite $\langle 100 \rangle$ direction and b) along the perovskite $\langle 011 \rangle$ direction.

STEM-HAADF-EELS

In order to provide further insight into the details of the nano size features and dislocations, atomically resolved STEM imaging and EELS measurements were performed. Firstly, the particle-void nature of the inclusions was independently confirmed by low loss EELS measurements of embedded nanoinclusions, demonstrating a drop in relative thickness (see Figure S3) consistent with the presence of a nano-void.

Figure 6 presents $[001]$ zone HAADF - EELS data from the core area of the L10 sample initially sintered in air prior to further annealing in Ar - 5%H₂ for 24 h. The horizontal and vertical directions in the image are aligned with the lattice directions of the perovskite structure. Figure 6a shows two sets of void-particle inclusions aligned in the same orientation with respect to each other, consistent with the SEM observation. In this particular case, both voids exhibit clear faceting; close up views (Figure 6b and 6c) show clearly how the

boundaries between the void and particle parts of the inclusion, and between the inclusion and the matrix, occur on [100] and [110] planes of the cubic structure of the L10 matrix. EELS elemental analysis from such an inclusion (marked with a rectangle in Figure 5a) reveals that the particle component of the inclusion is rich in Ti and O (Figure 6d,f) and depleted in Sr and La (Figure 6e,g) compared to the matrix (see also Figure S-4 in Supporting information).

The chemistry of the particle part of the inclusion can be further elucidated by looking at the near edge fine structure differences of the Ti $L_{2,3}$ and O K EELS edges from a particle/void and matrix area presented in Figure 7a. Figure 7b shows a Ti $L_{2,3}$ spectrum extracted from the $\text{Sr}_{0.9}\text{La}_{0.1}\text{TiO}_3$ matrix: the spectrum shows the characteristic white line shape of the edge, with the additional splitting of the L_3 and L_2 peaks into e_g , t_{2g} sub-components, corresponding to the Ti^{+4} octahedral coordination, as expected from SrTiO_3 type compounds^{50,51}. The matrix spectrum is plotted against a Ti $L_{2,3}$ spectrum extracted from the particle part of the inclusion. It can be readily seen that the e_g - t_{2g} splitting of the L_3 and L_2 peaks is far less pronounced, while the onset of the edge is slightly shifted to lower energies, indicating that the valence of Ti in the particle is reduced towards Ti^{+3} . Similarly, the near edge fine structure of the O K edge (Figure 7e) acquired from the particle region (Figure 7a) is significantly different from that of the matrix. The shape of the O K ELNES resembles that observed in highly O deficient SrTiO_3 samples, as well as those of mixed valence Ti_xO_y or Magneli type phases^{50,52}, in agreement with the Ti $L_{2,3}$ ELNES observation of a slightly lowered Ti valence. Additional HAADF images, elemental maps and relative thickness of void-particle pairs are presented in Figures S-5 and S-6 of the Supporting information. The experimental evidence suggests a strontium titanate phase with reduced Sr (La) content and Ti valence, and non-stoichiometry, with deficiency of Sr and O. EELS techniques were used to look for the presence of Boron; there was no evidence of Boron in the shell, the core or particles.

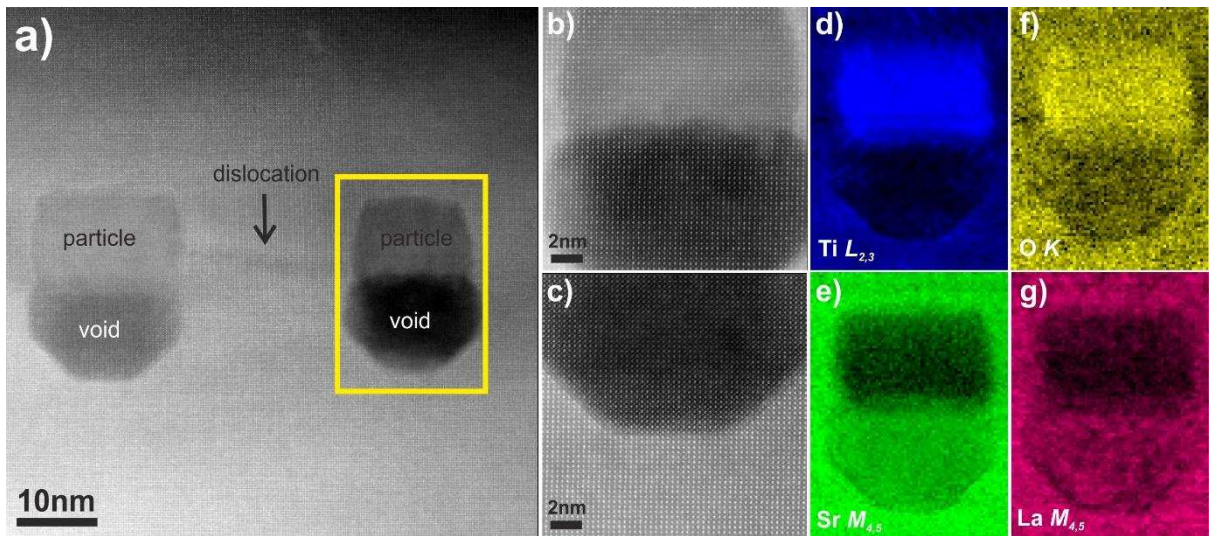


Figure 6. a) [001] zone axis HAADF STEM image of the L10 sample sintered in air then annealed in Ar - 5%H₂ for 24 h showing two sets of particle-void inclusions and b,c) HAADF STEM images showing the particle-void and void-matrix interfaces, respectively; d-g) EELS elemental maps produced using the Ti $L_{2,3}$, Sr $M_{4,5}$ and La $M_{4,5}$ ionisation edges, respectively

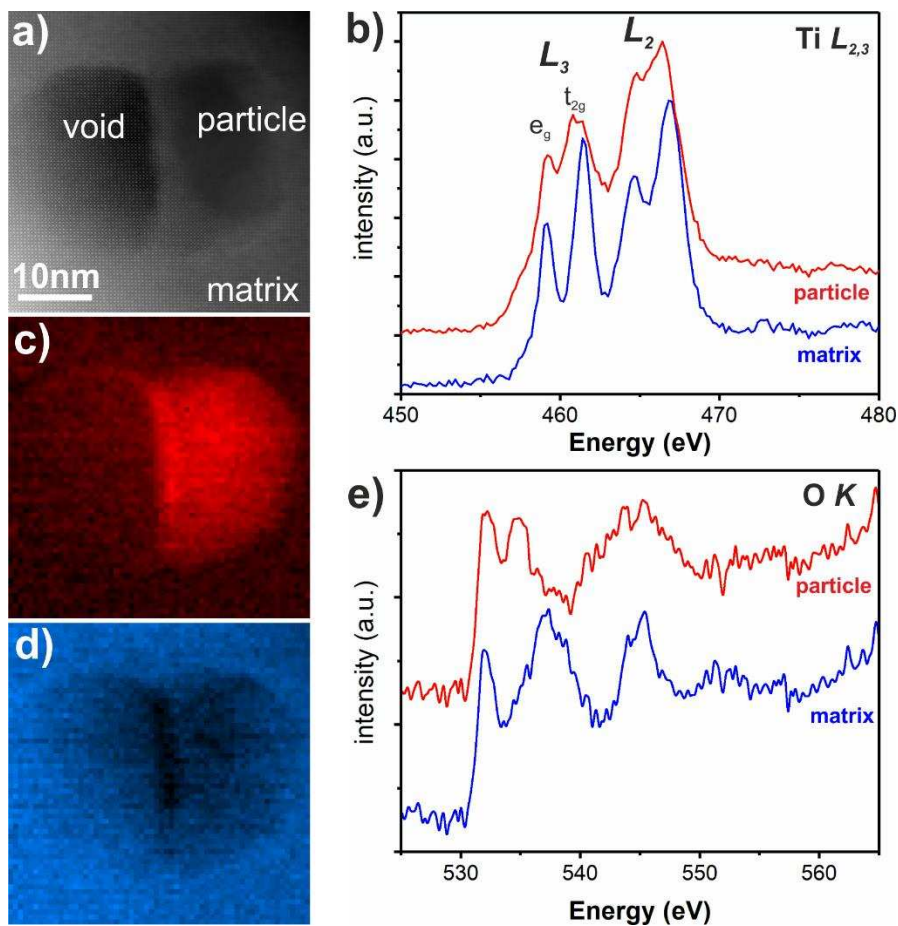


Figure 7. a) HAADF STEM image of a two-component inclusion in the L10 sample sintered in air then annealed in Ar - 5%H₂ for 24 h, b) Ti $L_{2,3}$ spectra, respectively extracted from the

particle component of the inclusion and the surrounding matrix. c, d) multi-linear least squares fit maps using spectra in b) as input references; e) O K spectra extracted from the particle component of the inclusion and the surrounding matrix, respectively.

As mentioned earlier, dislocations were observed in the core and shell areas of the sample. The nature of the dislocations was analysed using HAADF images by Fourier filtering to enhance the visibility of the location of the dislocation core (as presented in Figure 8a-c). The application of a Fourier filter on the (100) and (011) reflections from the image shown in Figure 8a, confirms the presence of a complex dislocation core: Figure 8b-c, consisting of combined (100) and (011) edge dislocations. This is similar to observations of dislocations in the Nd analogue of the same composition investigated in a separate study ($\text{Sr}_{0.9}\text{Nd}_{0.1}\text{TiO}_3$)³⁶. Advanced electron microscopy has provided chemical and structural details of these important microstructural features so we can now address their effects on the electrical and thermal transport properties of the $\text{Sr}_{0.9}\text{La}_{0.1}\text{TiO}_3$ ceramics.

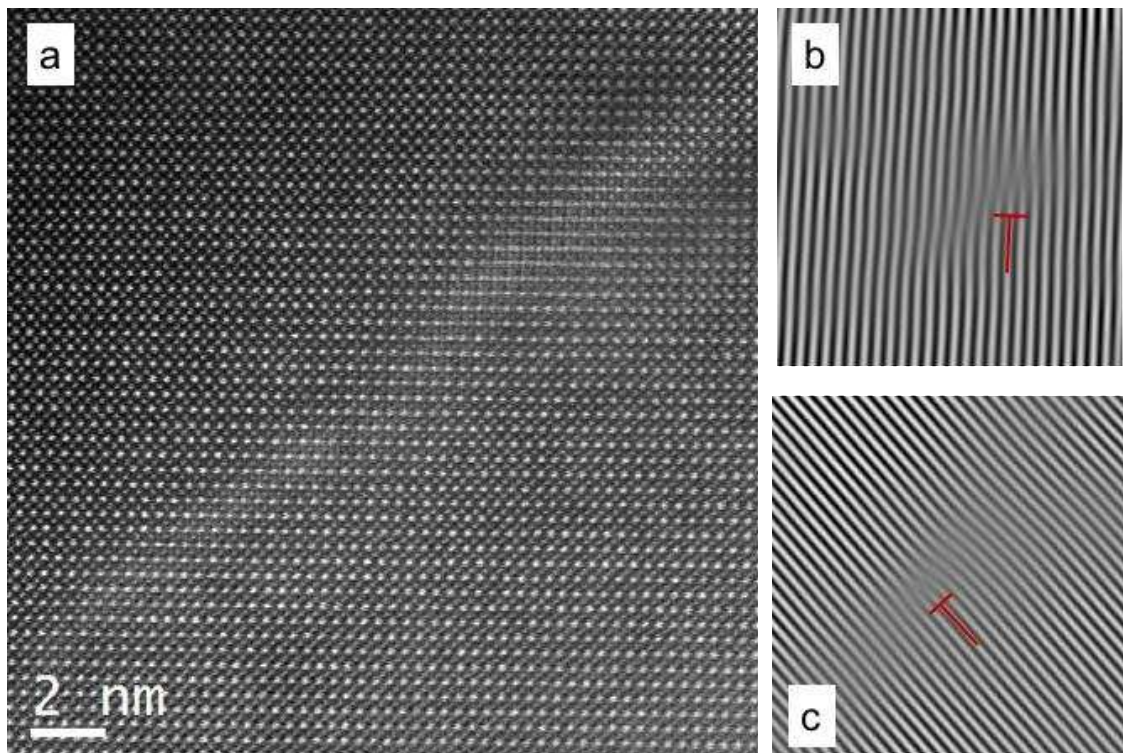


Figure 8. a) HAADF image; b) Fourier filtered version of the image selecting the (100) spots in Fourier space before applying an inverse Fourier transform; and c) Fourier filtered copy of a) using the (011) reflections. The dislocation cores are clearly highlighted with this procedure, and shown in (b) and (c) by red markers.

Thermoelectric Response

The air-sintered samples are, as expected, insulators and exhibit low electrical conductivity, consistent with the transport properties of other air-sintered strontium-titanate-based thermoelectrics³². Thus, the discussion will focus on the transport properties of samples annealed under reducing conditions. However, the discussion of thermal properties includes the air sintered sample as a reference baseline.

The transport properties of the samples are presented in Figure 9. Both electrical and thermal properties are dependent on annealing time. The annealed samples show semiconducting behaviour at low temperature changing to metallic behaviour at higher temperatures (Figure 9a). The electrical conductivity increases with annealing time, consistent with an increased concentration of Ti^{3+} ions (in turn generating additional carriers) suggested by the STEM-EELS results. It should be mentioned that the addition of boron may have had a positive role on the electrical conductivity of the annealed samples, as boron, when added to single-crystal SrTiO_3 , is known to behave as a charge carrier dopant, remarkably increasing electrical conductivity³⁸.

Although it is difficult to determine the exact structure and chemistry of the nano inclusions, the STEM-EELS data point towards a Ti rich structure, still containing Sr, and exhibiting high level of oxygen deficiency. This phase could be akin to a reduced ternary titanate or a Sr-doped TiO_x Magneli-type phase⁵³. The electrical conductivity of TiO_x -based Magneli phases is high, ranging from 800 S/cm to 300 S/cm at temperatures of 450 K to 1000 K, depending on the oxygen deficiency level^{54,55}. Therefore, particles of a similar nature within the microstructure would have a positive effect on the overall electrical conductivity. The pore components of the nano inclusions will, by comparison, have low electrical conductivity. However, since there is no significant reduction in the overall macroscopic density of the annealed samples, it would appear that the effect of voids on the overall electrical conductivity is minimal. Another microstructural feature that will influence electrical conductivity is the presence of dislocations. The full characterization of the types of dislocations present in these materials is beyond the scope of this study and requires further exploration. However, an atomistic simulation study of the role of $\langle 100 \rangle \{011\}$ edge dislocations, similar to that highlighted in Figure 8, on the defect chemistry and oxide ion transport properties of SrTiO_3 found that oxygen vacancies close to the dislocation core have lower formation energies⁵⁶. Thus dislocations facilitate the removal of oxygen from the

structure and aid the formation Ti^{3+} ions; in turn these are beneficial to the enhancement of the electrical conductivity⁵⁶. Additionally, dislocations (as structural defects) can contribute to phonon scattering and help to reduce thermal conductivity³⁶.

The absolute value of Seebeck coefficients range from 85 to 240 $\mu\text{V/K}$ in the temperature range 300 K to 1000 K and reduces systematically with increasing annealing time (Fig. 9b). As discussed above, this decrease is mainly attributed to an increase in carrier concentration, promoted by the reduction of Ti^{4+} to Ti^{3+} . The samples annealed for 24 h have the highest Seebeck coefficients amongst the highly conductive samples investigated and values are comparable with those for similar A-site doped SrTiO_3 thermoelectrics^{15,25}. Although an increase in Seebeck coefficients was reported by Li and Liu following the use of dispersed inclusions of nano SiC in the Bi_2Te_3 , they suggested that whilst the mechanism of enhancement was not known, the origin of the higher observed Seebeck coefficients was an energy filtering of low-energy carriers by low-energy defects associated with the nanovoids²⁹.

The combined effect of Seebeck coefficient and electrical conductivity on the thermoelectric response is embodied in the power factor ($S^2\sigma$). Data for the present samples are illustrated in Figure 9c. The power factor increases with temperature and peaks at 500 K to 600 K; this is typical for donor-doped strontium titanate⁵⁷. Samples annealed for 24h, 32h and 48h all showed high power factor values. The highest power factor of $1.6 \text{ mW m}^{-1} \text{ K}^{-1}$ was achieved at 550 K for samples annealed for 24 h. This is one of the highest values recorded for La doped SrTiO_3 ^{25,32,58,59}. As the samples annealed for 12 h show the lowest electrical conductivity, it is clear that the high Seebeck coefficients are responsible for the high power factor of the samples. The samples annealed for 12h showed the lowest power factor amongst the samples; consequently, full characterization was not conducted on this this sample.

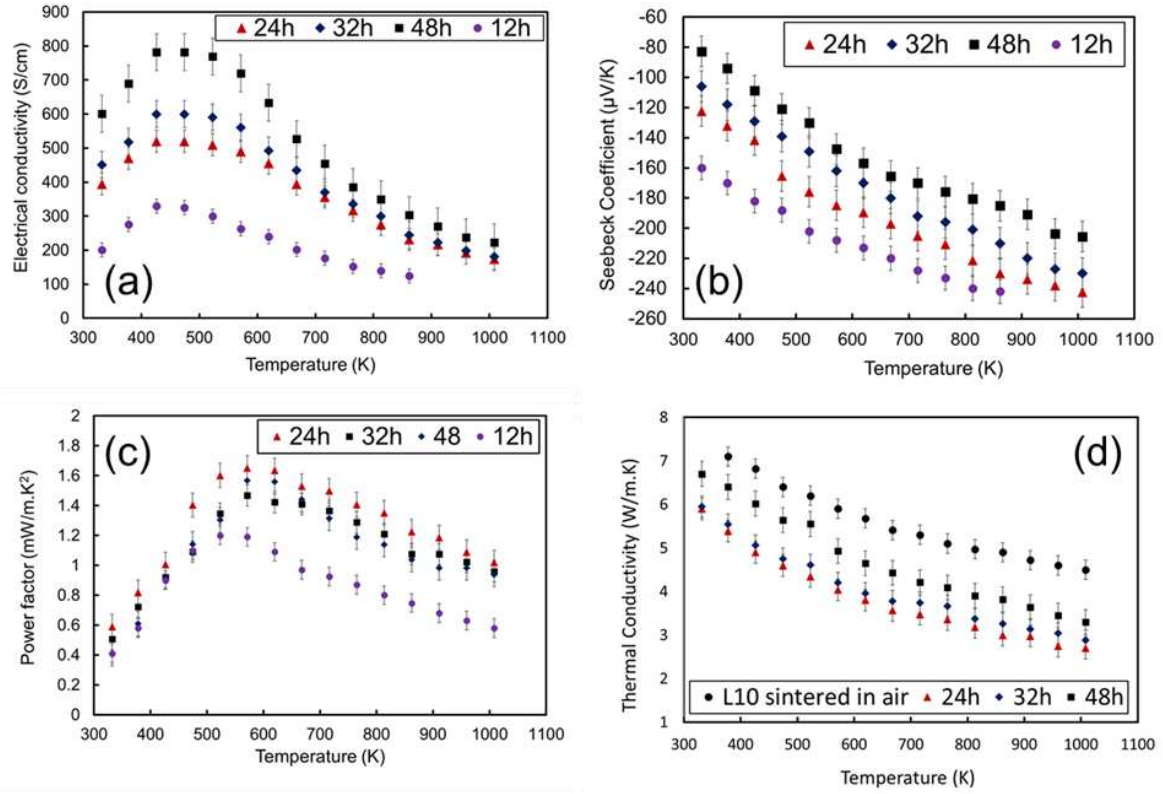


Figure 9 Temperature dependence of (a) Seebeck coefficient, (b) electrical conductivity, (c) power factor, and (d) total thermal conductivity for L10 samples (symbols: black ● represents samples sintered in air; symbols purple ●, red ▲, blue ◆, black ■ represent samples annealed under reducing conditions for 12 h, 24 h, 32 h, 48 h respectively).

To further understand the electrical conduction in the nanostructured samples, the carrier concentrations and mobility were calculated from the electrical conductivity and Seebeck coefficients. The carrier concentrations for the sample are calculated by the modified Hiekes' equation⁶⁰.

$$n = \left[\frac{A}{V} \right] \left[\frac{1}{e^S \frac{e}{k} + 1} \right] \quad (1)$$

where $\frac{A}{V}$ is the number of available sites for carrier per unit volume of the unit cell. For the cubic perovskite structure A is 1 and the V is the volume of the unit cell obtained from the refinement of the XRD data shown in Figure 1b. The factor e/k is the ratio of the electronic

charge (e) to the Boltzmann constant (k) and is approximately $0.011587 \mu\text{V/K}$. S is the Seebeck coefficient as shown in Figure 9b.

The modified Hiekes' equation is based on the assumption that only one electron is permitted on a given site and both degeneracies of spin and orbital are negligible ⁶⁰. The attribution of vibrational entropy part is also assumed to be 0. Therefore, the calculated values of carrier concentration are expected to be higher than the real values. The carrier mobility can be calculated from the carrier concentration and electrical conductivity (σ) using the following equation:

$$\mu = \sigma / (e \cdot n) \quad (2)$$

The calculated values for carrier concentration and charge mobility are shown in Table 1. The annealed L10 ceramics have high carrier concentrations in the range 2.3×10^{21} to $4.54 \times 10^{21} \text{ cm}^{-3}$ increasing with annealing time. Carrier mobility values are in the range 0.586 to 0.822 $\text{cm}^2\text{V}^{-1}\text{s}^{-1}$ increasing slightly with annealing time. The trends for carrier concentration and carrier mobility are a combined effect of nanostructuring and increased annealing time in the reducing atmosphere. The carrier concentration and mobility values reported here are in broad agreement with reported values for doped SrTiO_3 ceramics ^{31,36}.

Table 1. Carrier concentration and mobility for L10 samples annealed in Ar - 5% H₂ atmosphere for different times.

Sample	Carrier concentration (cm^{-3})	Carrier mobility ($\text{cm}^2\text{V}^{-1}\text{s}^{-1}$)
12 h	2.13×10^{21}	0.586
24 h	3.19×10^{21}	0.741
32 h	3.72×10^{21}	0.752
48 h	4.54×10^{21}	0.822

In spite of the high power factor, it is the high thermal conductivity of strontium titanate that limits its use for thermoelectric applications ²; a reduction of thermal conductivity is essential

for further improvement of the thermoelectric response of this material. The total thermal conductivity of the air sintered and the annealed samples are presented in Figure 9d. The air sintered samples show the expected very high thermal conductivity, typically $7.8 \text{ W m}^{-1} \text{ K}^{-1}$ at 350 K to $5.0 \text{ W m}^{-1} \text{ K}^{-1}$ at 1000 K, being slightly lower than that for un-doped polycrystalline, air-sintered strontium titanate³². In contrast the annealed samples show much lower thermal conductivity, with the 24 h samples exhibiting the lowest values across the temperature range, the minimum being $2.75 \text{ W m}^{-1} \text{ K}^{-1}$ at 1000 K. The lattice and electronic components of thermal conductivity (κ_{lattice} and $\kappa_{\text{electronic}}$) were calculated using the Wiedemann–Franz law, $\kappa_{\text{electronic}} = L\sigma T$, where L is the Sommerfeld value ($2.44 \times 10^{-8} \text{ W } \Omega \text{ K}^2$) of the Lorenz number⁶¹. The data are presented in Figure 10. The lattice component (Figure 10) dominates at all temperatures and falls with increasing measurement temperature and annealing time. The lowest lattice thermal conductivity of $2.25 \text{ W m}^{-1} \text{ K}^{-1}$ was achieved for the 24 h sample at 1000 K.

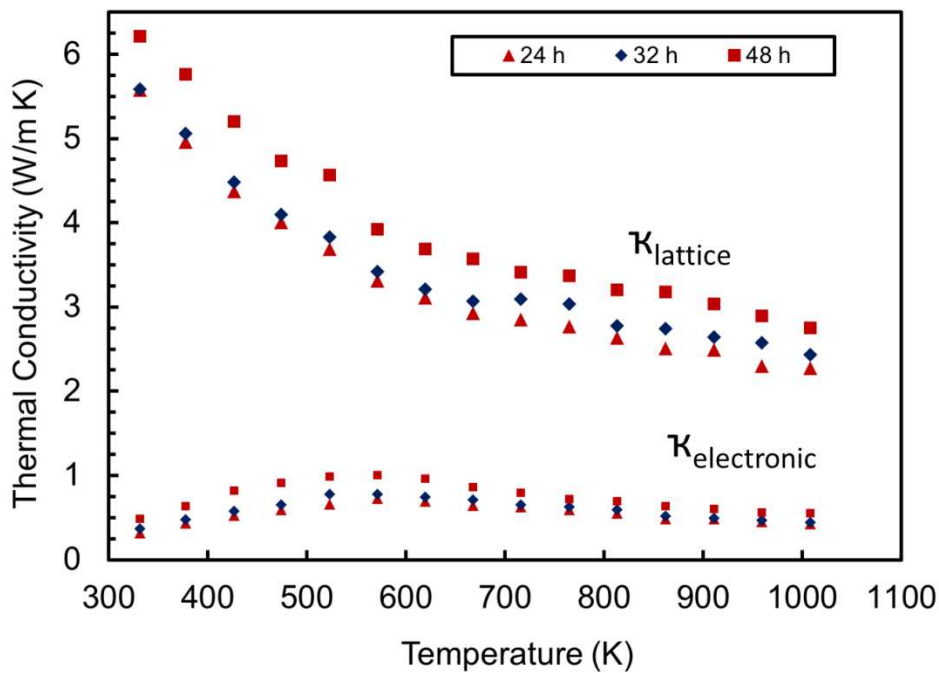


Figure 10. Temperature dependence of the lattice and electronic components of thermal conductivity components for $\text{Sr}_{0.9}\text{La}_{0.1}\text{TiO}_3$.

Perhaps the most effective role of nanostructuring in enhancing the performance of thermoelectrics is the reduction of the thermal conductivity^{11,29,62,63}. As highlighted in the introduction, SrTiO_3 has a high thermal conductivity at ambient and elevated temperatures. This is primarily due to the small mean free path for phonons $\sim 20 \text{ nm}$, as a result of the

simple cubic perovskite structure of SrTiO₃; thus reduction of lattice component of the thermal conductivity, K_{lattice} is essential. A number of approaches have been employed to reduce the thermal conductivity of SrTiO₃. Wang et al showed that reduction of the grain size from 20 μm to 55 nm greatly reduces the thermal conductivity in the temperature range 300 K to 1000 K; for example, from 4.5 W/m.K to 3.5 W/m.K at 1000 K⁶⁴. Wang et al fabricated composites of Nb-doped SrTiO₃ and yttria-stabilized zirconia (YSZ) with YSZ nanosized inclusions distributed at the grain boundaries and within the grains of Nb-doped SrTiO₃. The composite exhibited much lower thermal conductivity and it was suggested that the reduction was due to interface effects, specifically the enhanced scattering of phonons by the inclusions. Our results are a further illustration of the impact of nanosized features on thermal transport. Here the development of nanosized voids and inclusions are the primary reason for the reduction in the thermal conductivity in SrTiO₃. Additionally, the presence of other structural features generated by our new method of nanostructuring may contribute to the lowering of thermal conductivity; (i) the presence of dislocations in the shell and core. The numerous studies of the core structures of dislocations in SrTiO₃-based materials^{49,65-67} and our recent study of Sr_{0.9}Nd_{0.1}TiO₃ thermoelectric³⁶ has shown that a localised variation in the site occupancies, such as rearrangements of Ti-O octahedra and the appearance of Ti on Sr sites due to different types of configuration of edge sharing octahedra, can occur in the dislocation core regions. This localized chemical and structural variation and the associated defects in the vicinity of the dislocations will tend to reduce lattice thermal conductivity. (ii) The presence of core-shell type microstructures will encourage phonon scattering at their interfaces. (iii) The formation of oxygen vacancies in SrTiO₃ as a result of the reduction process, as demonstrated in the very recent work of Rahman et al.⁶⁸, generates additional phonon scattering centres to reduce thermal conductivity.

To explore the relationship between the size of the void-particle nanostructures and thermal conductivity, the size of the longest void-particle pairs in each of the samples (evaluated from the BSE-SEM images), and the lattice thermal conductivity at 1015 K were plotted against the annealing time spent in the reducing atmosphere (Figure 11). It can be seen that there is a direct correlation between lattice thermal conductivity and void-particle size; the smaller the size of the nano-sized features the lower the lattice thermal conductivity. This trend is valid for all the measurement temperatures for thermal conductivity. However, we do not have reliable data for the density of void-particle pairs in the different samples.

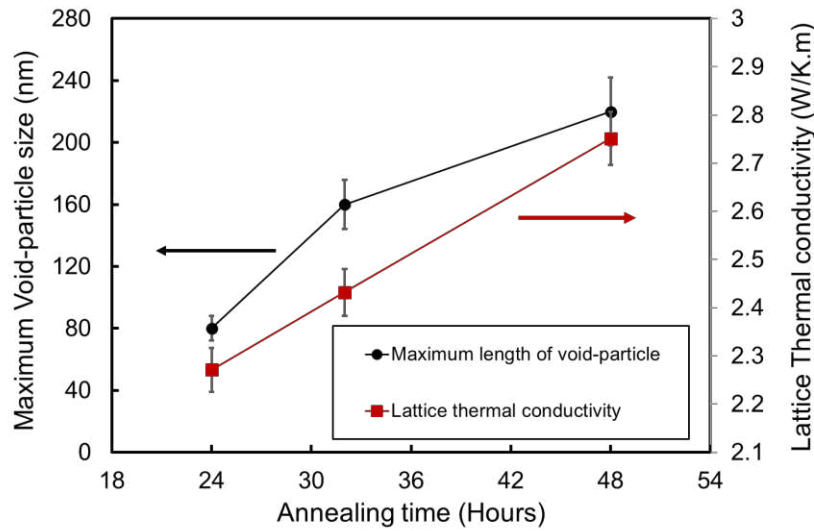


Figure 11. Maximum length of void-particle pair and lattice thermal conductivity at 1015 K as a function of sample annealing time.

The calculated thermoelectric figure of merit (ZT) based on values for the electronic and thermal transport properties (from Figure 8) are presented in Figure 12. It is clear that the microstructural development arising from increasing the annealing time led to a noticeable decrease in the thermal conductivity and increase in the Seebeck coefficient. The maximum ZT values achieved in this study for $\text{Sr}_{0.9}\text{La}_{0.1}\text{TiO}_3$ -based ceramics was 0.39 ± 0.03 at 1015 K. This is the highest determined ZT for $\text{Sr}_{0.9}\text{La}_{0.1}\text{TiO}_3$ compositions and one of the highest reported for any SrTiO_3 based thermoelectric³⁶.

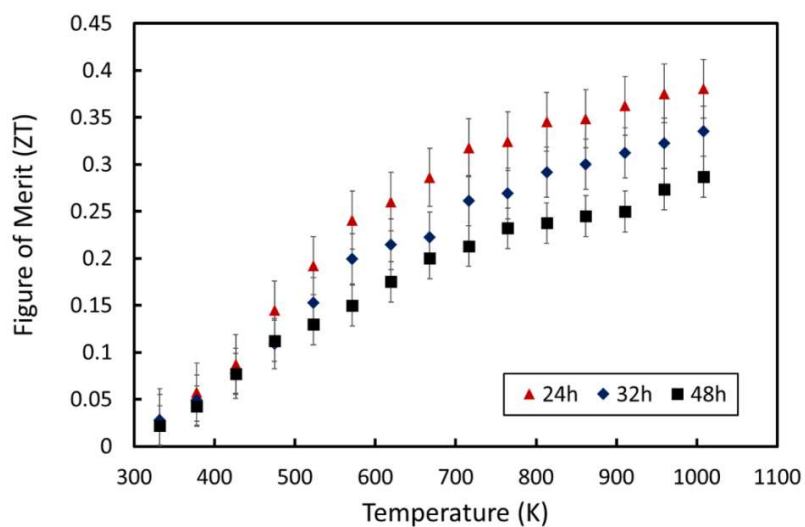


Figure 12. Temperature dependence of the thermoelectric figure of merit for $\text{Sr}_{0.9}\text{La}_{0.1}\text{TiO}_3$ samples annealed under reducing conditions.

Conclusions

We have established a new path towards engineering nanostructures in strontium titanate based thermoelectrics which may be applicable to other oxides. High density $\text{Sr}_{0.9}\text{La}_{0.1}\text{TiO}_3$ polycrystalline samples, with regular polygonal grains having a narrow grain size distribution and average size $\sim 7 \mu\text{m}$, were synthesised through liquid phase sintering by addition of boron and sintering in air atmosphere; they were then annealed in a reducing environment. This combined heat treatment led to the formation of a complex nano-structure within the grains.

X-ray diffraction confirmed $\text{Pm}\bar{3}\text{m}$ cubic crystal structure for all the samples. SEM revealed a core-shell type microstructure with the presence of nano-size features within the core area. HRTEM showed that the nano-size features are in the form of pairs of nano-sized voids and particles; their sizes depending on the annealing time. Atomic-resolution STEM-HAADF-EELS characterization in an aberration-corrected microscope showed that the precipitates are rich in Ti and the areas around the voids contain a high concentration of Ti^{3+} . Additionally, a high density of dislocations was observed in the shell areas; dislocations are also present in the core of the nano-structures, but with a lower density. Their presence may enhance electrical conductivity, although this aspect of the structure remains to be explored in more details.

The self-nano-structured $\text{Sr}_{0.9}\text{La}_{0.1}\text{TiO}_3$ ceramics showed a high power factor of $1600 \mu\text{W}/\text{m}\cdot\text{K}^2$ to $1050 \mu\text{W}/\text{m}\cdot\text{K}^2$ at temperatures of 600 K to 1015 K. However, the major impact of nano structuring was the reduction of thermal conductivity. Nano structured $\text{Sr}_{0.9}\text{La}_{0.1}\text{TiO}_3$ ceramics with shell size of ~ 1 micron and inclusions of 60 to 80 nm exhibit a low thermal conductivity of $\kappa = 2.75 \text{ W}/\text{m}\cdot\text{K}$ at 1015 K leading to a high of ZT of 0.39 ± 0.03 at this temperature. This is the highest ZT achieved for the highly studied $\text{Sr}_{0.9}\text{La}_{0.1}\text{TiO}_3$ composition^{15,25,26,34,59,69–71} and for other 10 mole % lanthanide doped SrTiO_3 thermoelectrics²⁵; a summary of published data is provided in Table S1. The study demonstrates a powerful nanostructuring strategy for significantly enhancing the performance of thermoelectric oxides; the approach could find much wider application in providing valuable guidance in the routes to synthesise future target materials.

Acknowledgments

The authors are grateful to the EPSRC for the provision of funding for this work (EP/H043462, EP/I036230/1, EP/L014068/1, EP/L017695/1 acknowledged by RF). SuperSTEM is the EPSRC National Research Facility for Advanced Electron Microscopy, and supported by EPSRC. All research data supporting this publication are directly available within the publication.

Supporting Information

Additional SEM images and EDS maps of Sr_{0.9}La_{0.1}TiO₃ ceramics, plus HAADF STEM images and EDS maps of void-particle inclusions within the ceramics, and related published ZT data are included as Supporting Information. This material is available free of charge from the publisher at <http://pubs.acs.org>.

References.

- (1) Chen, Z. G.; Hana, G.; Yanga, L.; Cheng, L.; Zou, J. Nanostructured Thermoelectric Materials: Current Research and Future Challenge. *Prog. Nat. Sci. Mater. Int.* **2012**, *22* (6), 535–549. <https://doi.org/10.1016/j.pnsc.2012.11.011>.
- (2) Koumoto, K.; Wang, Y.; Zhang, R.; Kosuga, A.; Funahashi, R. Oxide Thermoelectric Materials: A Nanostructuring Approach. *Annu. Rev. Mater. Res.* **2010**, *40* (1), 363–394. <https://doi.org/10.1146/annurev-matsci-070909-104521>.
- (3) Thermoelectric Nanomaterials: Design and Application; Komuto, K., Mori, T., Eds.; Springer, 2013. ISBN 978-3-642-37537-8
- (4) Alam, H.; Ramakrishna, S. A Review on the Enhancement of Figure of Merit from Bulk to Nano-Thermoelectric Materials. *Nano Energy* **2013**, *2* (2), 190–212. <https://doi.org/10.1016/j.nanoen.2012.10.005>.
- (5) Martín-González, M.; Caballero-Calero, O.; Díaz-Chao, P. Nanoengineering Thermoelectrics for 21st Century: Energy Harvesting and Other Trends in the Field. *Renew. Sustain. Energy Rev.* **2013**, *24*, 288–305. <https://doi.org/10.1016/j.rser.2013.03.008>.
- (6) Mori, T. Novel Principles and Nanostructuring Methods for Enhanced Thermoelectrics. *Small* **2017**, *13* (45), 1–10. <https://doi.org/10.1002/sml.201702013>.
- (7) Kanatzidis, M. G. Nanostructured Thermoelectrics: The New Paradigm? *Chem. Mater.* **2010**, *22* (3), 648–659. <https://doi.org/10.1021/cm902195j>.
- (8) Yeandel, S. R.; Molinari, M.; Parker, S. C. Nanostructuring Perovskite Oxides: The Impact of SrTiO₃nanocube 3D Self-Assembly on Thermal Conductivity. *RSC Adv.* **2016**, *6* (115), 114069–114077. <https://doi.org/10.1039/c6ra23887d>.
- (9) Neophytou, N.; Zianni, X.; Kosina, H.; Frabboni, S.; Lorenzi, B.; Narducci, D. Simultaneous Increase in Electrical Conductivity and Seebeck Coefficient in Highly Boron-Doped Nanocrystalline Si. *Nanotechnology* **2013**, *24* (20). <https://doi.org/10.1088/0957-4484/24/20/205402>.
- (10) Zebarjadi, M.; Esfarjani, K.; Bian, Z.; Shakouri, A. Low-Temperature Thermoelectric Power Factor Enhancement by Controlling Nanoparticle Size Distribution. *Nano Lett.* **2011**, *11* (1), 225–230. <https://doi.org/10.1021/nl103581z>.
- (11) Xie, W. J.; He, J.; Zhu, S.; Su, X. L.; Wang, S. Y.; Holgate, T.; Graff, J. W.; Ponnambalam,

- V.; Poon, S. J.; Tang, X. F.; Zhang, Q. J.; Tritt, T. M. Simultaneously Optimizing the Independent Thermoelectric Properties in (Ti,Zr,Hf)(Co,Ni)Sb Alloy by in Situ Forming InSb Nanoinclusions. *Acta Mater.* **2010**, 58 (14), 4705–4713. <https://doi.org/10.1016/j.actamat.2010.05.005>.
- (12) Jeng, M.-S.; Yang, R.; Song, D.; Chen, G. Modeling the Thermal Conductivity and Phonon Transport in Nanoparticle Composites Using Monte Carlo Simulation. *J. Heat Transfer* **2008**, 130 (4), 042410. <https://doi.org/10.1115/1.2818765>.
- (13) Li, J. F.; Liu, W. S.; Zhao, L. D.; Zhou, M. High-Performance Nanostructured Thermoelectric Materials. *NPG Asia Mater.* **2010**, 2 (4), 152–158. <https://doi.org/10.1038/asiamat.2010.138>.
- (14) Yu, M.; Saunders, T.; Grasso, S.; Mahajan, A.; Zhang, H.; Reece, M. J. Magnéli Phase Titanium Suboxides by Flash Spark Plasma Sintering. *Scr. Mater.* **2018**, 146, 241–245. <https://doi.org/10.1016/j.scriptamat.2017.11.044>.
- (15) Kikuchi, A.; Okinaka, N.; Akiyama, T. A Large Thermoelectric Figure of Merit of La-Doped SrTiO₃ prepared by Combustion Synthesis with Post-Spark Plasma Sintering. *Scr. Mater.* **2010**, 63 (4), 407–410. <https://doi.org/10.1016/j.scriptamat.2010.04.041>.
- (16) Yan, X.; Joshi, G.; Liu, W.; Lan, Y.; Wang, H.; Lee, S.; Simonson, J. W.; Poon, S. J.; Tritt, T. M.; Chen, G.; Ren, Z. F. Enhanced Thermoelectric Figure of Merit of P-Type Half-Heuslers. *Nano Lett.* **2011**, 11 (2), 556–560. <https://doi.org/10.1021/nl104138t>.
- (17) Zhou, X. W.; Jones, R. E. Effects of Nano-Void Density, Size and Spatial Population on Thermal Conductivity: A Case Study of GaN Crystal. *J. Phys. Condens. Matter* **2012**, 24 (32). <https://doi.org/10.1088/0953-8984/24/32/325804>.
- (18) Wang, N.; Chen, H.; He, H.; Norimatsu, W.; Kusunoki, M.; Koumoto, K. Enhanced Thermoelectric Performance of Nb-Doped SrTiO₃ by Nano-Inclusion with Low Thermal Conductivity. *Sci. Rep.* **2013**, 3 (1), 3449. <https://doi.org/10.1038/srep03449>.
- (19) Chen, L. D.; Huang, X. Y.; Zhou, M.; Shi, X.; Zhang, W. B. The High Temperature Thermoelectric Performances of Zr_{0.5}Hf_{0.5}Ni_{0.8}Pd_{0.2}Sn_{0.99}Sb_{0.01} Alloy with Nanophase Inclusions. *J. Appl. Phys.* **2006**, 99 (6). <https://doi.org/10.1063/1.2180432>.
- (20) Zhao, L. D.; Zhang, B. P.; Li, J. F.; Zhou, M.; Liu, W. S.; Liu, J. Thermoelectric and Mechanical Properties of Nano-SiC-Dispersed Bi₂Te₃ Fabricated by Mechanical Alloying and Spark Plasma Sintering. *J. Alloys Compd.* **2008**, 455 (1–2), 259–264. <https://doi.org/10.1016/j.jallcom.2007.01.015>.
- (21) Zhao, X. Y.; Shi, X.; Chen, L. D.; Zhang, W. Q.; Bai, S. Q.; Pei, Y. Z.; Li, X. Y.; Goto, T. Synthesis of Yb_yCo₄Sb₁₂/Yb₂O₃ Composites and Their Thermoelectric Properties. *Appl. Phys. Lett.* **2006**, 89 (9), 10–13. <https://doi.org/10.1063/1.2345249>.
- (22) Sootsman, J. R.; Kong, H.; Uher, C.; D'Angelo, J. J.; Wu, C. I.; Hogan, T. P.; Caillat, T.; Kanatzidis, M. G. Large Enhancements in the Thermoelectric Power Factor of Bulk PbTe at High Temperature by Synergistic Nanostructuring. *Angew. Chemie - Int. Ed.* **2008**, 47 (45), 8618–8622. <https://doi.org/10.1002/anie.200803934>.
- (23) Li, H.; Tang, X.; Su, X.; Zhang, Q. Preparation and Thermoelectric Properties of High-Performance Sb Additional Yb_{0.2}Co₄Sb_{12+y} Bulk Materials with Nanostructure. *Appl. Phys. Lett.* **2008**, 92 (20). <https://doi.org/10.1063/1.2936277>.
- (24) Wang, H.; Su, W.; Liu, J.; Wang, C. Recent Development of N-Type Perovskite Thermoelectrics. *J. Mater.* **2016**, 2 (3), 225–236. <https://doi.org/10.1016/j.jmat.2016.06.005>.
- (25) Kovalevsky, A. V.; Yaremchenko, A. A.; Populoh, S.; Thiel, P.; Fagg, D. P.; Weidenkaff, A.; Frade, J. R. Towards a High Thermoelectric Performance in Rare-Earth Substituted SrTiO₃: Effects Provided by Strongly-Reducing Sintering Conditions. *Phys. Chem. Chem. Phys.* **2014**, 16 (48), 26946–26954. <https://doi.org/10.1039/c4cp04127e>.
- (26) Shang, P. P.; Zhang, B. P.; Liu, Y.; Li, J. F.; Zhu, H. M. Preparation and Thermoelectric Properties of La-Doped SrTiO₃ Ceramics. *J. Electron. Mater.* **2011**, 40 (5), 926–931. <https://doi.org/10.1007/s11664-010-1452-5>.
- (27) Buscaglia, M. T.; Maglia, F.; Anselmi-Tamburini, U.; Marré, D.; Pallecchi, I.; Ianculescu, A.; Canu, G.; Viviani, M.; Fabrizio, M.; Buscaglia, V. Effect of Nanostructure on the Thermal Conductivity of La-Doped SrTiO₃ Ceramics. *J. Eur. Ceram. Soc.* **2014**, 34 (2), 307–316. <https://doi.org/10.1016/j.jeurceramsoc.2013.08.009>.
- (28) Wang, Y.; Fujinami, K.; Zhang, R.; Wan, C.; Wang, N.; Ba, Y.; Koumoto, K. Interfacial

- Thermal Resistance and Thermal Conductivity in Nanograined SrTiO₃. *Appl. Phys. Express* **2010**, 3 (3), 2–5. <https://doi.org/10.1143/APEX.3.031101>.
- (29) Li, J. F.; Liu, J. Effect of Nano-SiC Dispersion on Thermoelectric Properties of Bi₂Te₃ Polycrystals. *Phys. Status Solidi Appl. Mater. Sci.* **2006**, 203 (15), 3768–3773. <https://doi.org/10.1002/pssa.200622011>.
- (30) Srivastava, D.; Norman, C.; Azough, F.; Schäfer, M. C.; Guilmeau, E.; Freer, R. Improving the Thermoelectric Properties of SrTiO₃-Based Ceramics with Metallic Inclusions. *J. Alloys Compd.* **2018**, 731, 723–730. <https://doi.org/10.1016/j.jallcom.2017.10.033>.
- (31) Srivastava, D.; Norman, C.; Azough, F.; Schäfer, M. C.; Guilmeau, E.; Kepaptsoglou, D.; Ramasse, Q. M.; Nicotra, G.; Freer, R. Tuning the Thermoelectric Properties of A-Site Deficient SrTiO₃ Ceramics by Vacancies and Carrier Concentration. *Phys. Chem. Chem. Phys.* **2016**, 18 (38), 26475–26486. <https://doi.org/10.1039/c6cp05523k>.
- (32) Azough, F.; Jackson, S. S.; Ekren, D.; Freer, R.; Molinari, M.; Yeandel, S. R.; Panchmatia, P. M.; Parker, S. C.; Maldonado, D. H.; Kepaptsoglou, D. M.; Ramasse, Quentin M. Concurrent La and A-Site Vacancy Doping Modulates the Thermoelectric Response of SrTiO₃: Experimental and Computational Evidence. *ACS Appl. Mater. Interfaces* **2017**, 9 (48), 41988–42000. <https://doi.org/10.1021/acsami.7b14231>.
- (33) Wang, J.; Zhang, B. Y.; Kang, H. J.; Li, Y.; Yaer, X.; Li, J. F.; Tan, Q.; Zhang, S.; Fan, G. H.; Liu, C. Y.; Miao, L.; Nan, D.; Wang, T. M.; Zhao, I. D. Record High Thermoelectric Performance in Bulk SrTiO₃ via Nano-Scale Modulation Doping. *Nano Energy* **2017**, 35 (January), 387–395. <https://doi.org/10.1016/j.nanoen.2017.04.003>.
- (34) Okinaka, N.; Zhang, L.; Akiyama, T. Thermoelectric Properties of Rare Earth-Doped SrTiO₃ Using Combination of Combustion Synthesis (CS) and Spark Plasma Sintering (SPS). *ISIJ Int.* **2010**, 50 (9), 1300–1304. <https://doi.org/10.2355/isijinternational.50.1300>.
- (35) Obara, H.; Yamamoto, A.; Lee, C. H.; Kobayashi, K.; Matsumoto, A.; Funahashi, R. Thermoelectric Properties of Y-Doped Polycrystalline SrTiO₃. *Japanese J. Appl. Physics, Part 2 Lett.* **2004**, 43 (4 B), 540–542. <https://doi.org/10.1143/JJAP.43.L540>.
- (36) Ekren, D.; Azough, F.; Gholinia, A.; Day, S. J.; Hernandez-Maldonado, D.; Kepaptsoglou, D. M.; Ramasse, Q. M.; Freer, R. Enhancing the Thermoelectric Power Factor of Sr_{0.9}Nd_{0.1}TiO₃ through Control of the Nanostructure and Microstructure. *J. Mater. Chem. A* **2018**, 6 (48), 24928–24939. <https://doi.org/10.1039/C8TA07861K>.
- (37) Rhim, S. M.; Hong, S.; Bak, H.; Kim, O. K. Effects of B₂O₃ Addition on the Dielectric and Ferroelectric Properties of Ba_{0.7}Sr_{0.3}TiO₃ Ceramics. *J. Am. Ceram. Soc.* **2000**, 83 (5), 1145–1148. <https://doi.org/10.1111/j.1151-2916.2000.tb01345.x>.
- (38) Okamoto, J.; Shimizu, G.; Kubo, S.; Yamada, Y.; Kitagawa, H.; Matsushita, A.; Yamada, Y.; Ishikawa, F. Thermoelectric Properties of B-Doped SrTiO₃ Single Crystal. *J. Phys. Conf. Ser.* **2009**, 176, 012042. <https://doi.org/10.1088/1742-6596/176/1/012042>.
- (39) Coelho, A. A. Whole-Profile Structure Solution from Powder Diffraction Data Using Simulated Annealing. *J. Appl. Crystallogr.* **2000**, 33, 899–908.
- (40) Palatinus, L.; Brázda, P.; Jelínek, M.; Hrdá, J.; Steciuk, G.; Klementová, M. PETS 2.0: Computer Program for Processing of Electron Diffraction Tomography Data. *Acta Crystallogr. B* **2019**, Accepted.
- (41) Prosandeev, S. A.; Raevski, I. P.; Bunin, M. A. Comment on “Conduction States in Oxide Perovskites: Three Manifestations of Ti³⁺ Jahn-Teller Polarons in Barium Titanate.” *Phys. Rev. B* **2004**, 70 (15), 157101. <https://doi.org/10.1103/PhysRevB.70.157101>.
- (42) Shannon, R. D. No Title. *Acta Crystallogr.* **1976**, A32, 751–767.
- (43) Lu, Z.; Zhang, H.; Lei, W.; Sinclair, D. C.; Reaney, I. M. High-Figure-of-Merit Thermoelectric La-Doped A-Site-Deficient SrTiO₃ Ceramics. *Chem. Mater.* **2016**, 28 (3), 925–935. <https://doi.org/10.1021/acs.chemmater.5b04616>.
- (44) Elcombe, M. M.; Kisi, E. H.; Hawkins, K. D.; White, T. J.; Goodman, P.; Matheson, S. Structure Determinations for Ca₃Ti₂O₇, Ca₄Ti₃O₁₀, Ca_{3.6}Sr_{0.4}Ti₃O₁₀ and a Refinement of Sr₃Ti₂O₇. *Acta Crystallogr. Sect. B* **1991**, 47 (3), 305–314. <https://doi.org/10.1107/S0108768190013416>.
- (45) Wei, Z. ; Chen, X. ; Wang, F. ; Li, W. ; He, M.; Zhang, Y. Phase Relations in the Ternary System SrO–TiO₂–B₂O₃. *J. Alloys Compd.* **2001**, 327 (1–2), L10–L13.

- [https://doi.org/10.1016/s0925-8388\(01\)01564-x](https://doi.org/10.1016/s0925-8388(01)01564-x).
- (46) Drys, M.; Trzebiatowski, W. The System Strontium Oxide-Titanium Dioxide. *Rocz. Chem.* **1957**, 31 (2), 489–496.
 - (47) Lee, S. B.; Sigle, W.; Phillipp, F.; Brunner, D. In Situ High-Resolution Transmission Electron Microscopy of Dislocation Formation and Dynamics during the Crystallization of Amorphous SrTiO₃. *Acta Materialia*. 2005, pp 1843–1848. <https://doi.org/10.1016/j.actamat.2004.12.034>.
 - (48) Matsunaga, T.; Saka, H. Transmission Electron Microscopy of Dislocations in SrTiO₃. *Philos. Mag. Lett.* **2000**, 80 (9), 597–604. <https://doi.org/10.1080/09500830050134309>.
 - (49) Du, H.; Jia, C. L.; Houben, L.; Metlenko, V.; De Souza, R. A.; Waser, R.; Mayer, J. Atomic Structure and Chemistry of Dislocation Cores at Low-Angle Tilt Grain Boundary in SrTiO₃ Bicrystals. *Acta Mater.* **2015**, 89, 344–351. <https://doi.org/10.1016/j.actamat.2015.02.016>.
 - (50) Stoyanov, E.; Langenhorst, F.; Steinle-Neumann, G. The Effect of Valence State and Site Geometry on Ti L_{3,2} and O K Electron Energy-Loss Spectra of Ti_xO_y Phases. *Am. Mineral.* **2007**, 92 (4), 577–586. <https://doi.org/10.2138/am.2007.2344>.
 - (51) Brydson, R.; Williams, B. G.; Engel, W.; Sauer, H.; Zeitler, E. Electron Energy-Loss Spectroscopy (EELS) and the Electronic Structure of Titanium Dioxide. *Solid State Commun.* **1987**, 64 (4), 609–612.
 - (52) D. A. Muller, N. Nakagawa, A. Ohtomo, J. A. G. and H. Y. H. Atomic scale imaging of nanoengineered oxygen profiles in SrTiO₃. *Nature* **2004**, 430, 657–661.
 - (53) Hessen, B.; Sunshine, S. A.; Siegrist, T. New Reduced Ternary Titanates from Borate Fluxes. *J. Solid State Chem.* **1991**, 94 (2), 306–312. [https://doi.org/10.1016/0022-4596\(91\)90196-O](https://doi.org/10.1016/0022-4596(91)90196-O).
 - (54) Backhaus-Ricoult, M.; Rustad, J. R.; Vargheese, D.; Dutta, I.; Work, K. Levers for Thermoelectric Properties in Titania-Based Ceramics. *J. Electron. Mater.* **2012**, 41 (6), 1636–1647. <https://doi.org/10.1007/s11664-012-2019-4>.
 - (55) Pandey, S. J.; Joshi, G.; Wang, S.; Curtarolo, S.; Gaume, R. Thermoelectric Characterization of Fine-Grained Ti₅O₉ Magneli Phase Ceramics. *arXiv Prepr. arXiv1602.07747* **2016**.
 - (56) Marrocchelli, D.; Sun, L.; Yildiz, B. Dislocations in SrTiO₃: Easy to Reduce but Not so Fast for Oxygen Transport. *J. Am. Chem. Soc.* **2015**, 137 (14), 4735–4748. <https://doi.org/10.1021/ja513176u>.
 - (57) Teranishi, T.; Ishikawa, Y.; Hayashi, H.; Kishimoto, A.; Katayama, M.; Inada, Y. Thermoelectric Efficiency of Reduced SrTiO₃ Ceramics Modified with La and Nb. *J. Am. Ceram. Soc.* **2013**, 96 (9), 2852–2856. <https://doi.org/10.1111/jace.12379>.
 - (58) Sun, Y.; Wang, C. L.; Wang, H. C.; Peng, H.; Guo, F. Q.; Su, W. B.; Liu, J.; Li, J. C.; Mei, L. M. Yttrium-Doped Effect on Thermoelectric Properties of La_{0.1}Sr_{0.9}TiO₃ Ceramics. *J. Mater. Sci.* **2011**, 46 (15), 5278–5281. <https://doi.org/10.1007/s10853-011-5466-z>.
 - (59) Liu, J.; Wang, C. L.; Su, W. B.; Wang, H. C.; Zheng, P.; Li, J. C.; Zhang, J. L.; Mei, L. M. Enhancement of Thermoelectric Efficiency in Oxygen-Deficient Sr_{1-x}La_xTiO_{3-δ} Ceramics. *Appl. Phys. Lett.* **2009**, 95 (16), 2009–2012. <https://doi.org/10.1063/1.3254219>.
 - (60) Taguchi, H.; Sonoda, M.; Nagao, M. Relationship between Angles for Mn–O–Mn and Electrical Properties of Orthorhombic Perovskite-Type (Ca_{1-x}Sr_x)MnO₃. *J. Solid State Chem.* **1998**, 137 (1), 82–86. <https://doi.org/10.1006/jssc.1997.7701>.
 - (61) Chester, G. V.; Thellung, A. The Law of Wiedemann and Franz. *Proc. Phys. Soc.* **1961**, 77 (5), 1005–1013. <https://doi.org/10.1088/0370-1328/77/5/309>.
 - (62) Xiong, Z.; Chen, X.; Zhao, X.; Bai, S.; Huang, X.; Chen, L. Effects of Nano-TiO₂ Dispersion on the Thermoelectric Properties Offilled-Skutterudite Ba_{0.22}Co₄Sb₁₂. *Solid State Sci.* **2009**, 11 (9), 1612–1616. <https://doi.org/10.1016/j.solidstatesciences.2009.06.007>.
 - (63) Ohtaki, M.; Hayashi, R.; Araki, K.; Agency, T. Thermoelectric Properties of Sintered ZnO Incorporating Nanovoid Structure : Influence of the Size and Number Density of Nanovoids (a) b) c) D). *Int. Conf. Thermoelectr.* **2007**, 112–117.
 - (64) Wang, Y.; Fujinami, K.; Zhang, R.; Wan, C.; Wang, N.; Ba, Y.; Koumoto, K. Interfacial Thermal Resistance and Thermal Conductivity in Nanograined SrTiO₃. *Appl. Phys. Express* **2010**, 3 (3), 5–7. <https://doi.org/10.1143/APEX.3.031101>.
 - (65) Gao, P.; Ishikawa, R.; Feng, B.; Kumamoto, A.; Shibata, N.; Ikuhara, Y. Atomic-Scale Structure Relaxation, Chemistry and Charge Distribution of Dislocation Cores in SrTiO₃. *Ultramicroscopy* **2018**, 184, 217–224. <https://doi.org/10.1016/j.ultramic.2017.09.006>.

- (66) Kim, H. S.; Kang, S. D.; Tang, Y.; Hanus, R.; Jeffrey Snyder, G. Dislocation Strain as the Mechanism of Phonon Scattering at Grain Boundaries. *Mater. Horizons* **2016**, 3 (3), 234–240. <https://doi.org/10.1039/c5mh00299k>.
- (67) De Souza, R.; Fleig, J.; Maier, J.; Kienzle, O.; Zhang, Z.; Sigle, W.; Rühle, M. Electrical and Structural Characterization of a Low-Angle Tilt Grain Boundary in Iron-Doped Strontium Titanate. *J. Am. Ceram. Soc.* **2003**, 86 (6), 922–928. <https://doi.org/10.1111/j.1151-2916.2003.tb03398>.
- (68) Rahman, J. U.; Nam, W. H.; Van Du, N.; Rahman, G.; Rahman, A. U.; Shin, W. H.; Seo, W. S.; Kim, M. H.; Lee, S. Oxygen Vacancy Revived Phonon-Glass Electron-Crystal in SrTiO₃. *J. Eur. Ceram. Soc.* **2019**, 39 (2–3), 358–365. <https://doi.org/10.1016/j.jeurceramsoc.2018.09.036>.
- (69) Wang, H. C.; Wang, C. L.; Su, W. B.; Liu, J.; Peng, H.; Sun, Y.; Zhang, J. L.; Zhao, M. L.; Li, J. C.; Yin, N.; et al. Synthesis and Thermoelectric Performance of Ta Doped Sr_{0.9}La_{0.1}TiO₃ Ceramics. *Ceram. Int.* **2011**, 37 (7), 2609–2613. <https://doi.org/10.1016/j.ceramint.2011.04.004>.
- (70) Liu, J.; Wang, C. L.; Li, Y.; Su, W. B.; Zhu, Y. H.; Li, J. C.; Mei, L. M. Influence of Rare Earth Doping on Thermoelectric Properties of SrTiO₃ Ceramics. *J. Appl. Phys.* **2013**, 114 (22). <https://doi.org/10.1063/1.4847455>.
- (71) Park, K.; Son, J. S.; Woo, S. I.; Shin, K.; Oh, M. W.; Park, S. D.; Hyeon, T. Colloidal Synthesis and Thermoelectric Properties of La-Doped SrTiO₃ Nanoparticles. *J. Mater. Chem. A* **2014**, 2 (12), 4217–4224. <https://doi.org/10.1039/c3ta14699e>.